

Primordial black holes and induced gravitational waves from logarithmic non-Gaussianity

Ryoto Inui,^a Cristian Joana,^b Hayato Motohashi,^c Shi Pi,^{b,d,e}
Yuichiro Tada,^{a,f} and Shuichiro Yokoyama^{g,a,e}

^aDepartment of Physics, Nagoya University, Furo-cho Chikusa-ku, Nagoya 464-8602, Japan

^bCAS Key Laboratory of Theoretical Physics, Institute of Theoretical Physics, Chinese Academy of Sciences, Beijing 100190, China

^cDivision of Liberal Arts, Kogakuin University, 2665-1 Nakano-machi, Hachioji, Tokyo, 192-0015, Japan

^dCenter for High Energy Physics, Peking University, Beijing 100871, China

^eKavli Institute for the Physics and Mathematics of the Universe (WPI), UTIAS, The University of Tokyo, Kashiwa, Chiba 277-8583, Japan

^fInstitute for Advanced Research, Nagoya University, Furo-cho Chikusa-ku, Nagoya 464-8601, Japan

^gKobayashi Maskawa Institute, Nagoya University, Chikusa, Aichi 464-8602, Japan

E-mail: inui.ryoto.a3@s.mail.nagoya-u.ac.jp, cristian.joana@itp.ac.cn,
motohashi@cc.kogakuin.ac.jp, shi.pi@itp.ac.cn,
tada.yuichiro.y8@f.mail.nagoya-u.ac.jp, shu@kmi.nagoya-u.ac.jp

Abstract. We investigate the formation of primordial black hole (PBH) based on numerical relativity simulations and peak theory as well as the corresponding scalar induced gravitational wave (SIGW) signals in the presence of *logarithmic non-Gaussianities* which has recently been confirmed in a wide class of inflation models. Through numerical calculations, we find certain parameter spaces of the critical thresholds for the type A PBH formation and reveal a maximum critical threshold value. We also find that there is a region where no PBH is produced from type II fluctuations contrary to a previous study. We then confirm that SIGW signals originated from the logarithmic non-Gaussianity are detectable in the Laser Interferometer Space Antenna if PBHs account for whole dark matter. Finally, we discuss the SIGW interpretation of the nHz stochastic gravitational wave background reported by the recent pulsar timing array observations. We find that PBH overproduction is a serious problem for most of the parameter space, while this tension might still be alleviated in the non-perturbative regime.

Contents

1	Introduction	1
2	PBH formation with the logarithmic non-Gaussianity	2
2.1	Peak profile	3
2.2	The Compaction function	4
2.3	The q -function method	5
2.4	Numerical study on the thresholds	6
2.5	Abundance of PBHs	6
3	The scalar induced gravitational wave signals	10
3.1	Formulation	10
3.2	SIGW associated with PBH dark matter	13
3.3	SIGW in light of recent PTA results	13
4	Conclusions	15
A	The convergence of the scalar-induced gravitational waves	17
B	The BSSN formalism of Numerical Relativity	18
B.1	Gravitational hydrodynamics	20

1 Introduction

Primordial black holes (PBHs) are hypothetical compact objects that might have been formed in the early universe [1, 2]. Although various formation scenarios have been discussed (e.g., the formation in the matter-dominated universe [3], the formation from the isocurvature perturbation [4, 5], and the formation from a resonant instability of cosmological perturbation during a preheating [6, 7]), the widely discussed one is the gravitational collapse of the highly dense regions in the radiation-dominated universe. PBHs can be formed in a wide range of masses unlike astrophysical black holes, and they can provide a sizable amount of dark matter (DM). The mass range between $[10^{-15}M_{\odot}-10^{-11}M_{\odot}]$ is often called the *PBH Dark Matter window* because it can account for all the DM according to the current observational constraints [8–10]. PBHs are not only promising DM candidates but can also potentially explain other cosmological and astrophysical phenomena. For instance, they could constitute the seeds for the supermassive black holes in galactic nuclei or galaxies [11], be relevant sources of gravitational wave (GW) events in ground-based detectors [12–15] and in pulsar timing array (PTA) observations [16–19], have a role on explaining baryogenesis [20–22], and even stand as the exotic object present in the solar system [23, 24].

In addition to these motivations, recently, more precise studies focusing on the relationship between GWs and PBHs have been actively discussed (see, e.g., Ref. [25]). The large primordial perturbations necessary for PBH formation can induce GWs through the second-order interactions between the scalar and tensor metric perturbations. The frequency of GWs is related to the PBH mass, as both of them depend on the size of the Hubble horizon at the reentry. In particular, our main interest relies on the mass band of the PBH mass window

corresponding to the frequency band of space-borne interferometers, such as Laser Interferometer Space Antenna (LISA) [26], Deci-hertz Gravitational Wave Observatory (DECIGO) [27], Taiji [28], and TianQin [29]. In fact, it was pointed out that LISA can detect the scalar induced gravitational wave (SIGW) signal when the PBHs in the mass range of the DM window occupy the entire DM [30, 31]. Interestingly, the detectability of milihertz SIGW is robust against non-Gaussianity, which has also been widely studied [30, 32–35].

On the theoretical side, recently, the curvature perturbations ζ having a non-Gaussian exponential tail in their probability density function have come to be discussed [36–39]. One typical model that realizes such a non-Gaussian curvature perturbation is the ultra slow-roll inflation. The primordial curvature perturbation produced during the ultra slow-roll phase could have sufficiently large amplitudes for PBH formations and have an *exponential-tail* distribution which asymptotically follows $P(\zeta) \propto \exp(-3\zeta)$ in the large ζ limit. It is explained by the logarithmic relation $\zeta = -(1/3) \ln(1 - 3\zeta_g)$ between the curvature perturbation ζ and a certain Gaussian random field ζ_g . A more general form of a logarithmic type curvature perturbation can be expressed as $\zeta = -(1/\gamma) \ln(1 - \gamma\zeta_g)$ with a constant parameter γ . We call this the *logarithmic non-Gaussianity* relation. This logarithmic non-Gaussianity can be found in a class of the constant roll inflation model which is the generalized model of the ultra slow-roll inflation [40–44], as well as in the curvaton scenario [45]. In the constant roll scenario, the primordial scalar power spectrum can be blue-tilted and it could realize the efficient PBH formation [46–52]. The probability density function of the logarithmic type curvature perturbations has the exponential tail $P(\zeta) \propto \exp(-\gamma\zeta)$ for $\gamma > 0$, and follows the *Gumbel* tail as $P(\zeta) \propto \exp\left(-\frac{1}{2\gamma^2\sigma^2}e^{-2\gamma\zeta}\right)$ with the variance $\sigma^2 = \langle \zeta_g^2 \rangle$ for $-3/2 < \gamma < 0$ [42, 44]. Although the influence of the exponential tail in the ultra slow-roll model (i.e., $\gamma = 3$) on the PBH formation and the corresponding SIGW signals have been studied in Refs. [34, 53], the PBH formation and the related SIGW signals in general parameter space are unknown. Additionally, as PBHs may be overproduced when trying to explain the nHz SGWB observed by PTAs as induced by the curvature perturbation [16], a negative non-Gaussianity is implied [54]. This also motivates us to study the PBH formation in the logarithmic non-Gaussianity with $\gamma < 0$.

In this work, we investigate the PBH formation when there is logarithmic non-Gaussianity, based on the numerical relativity and peak theory. The corresponding SIGW spectrum is also calculated analytically. This paper is organized as follows. We describe the process of PBH formation including the considered peak profile, threshold estimation, and computation of abundances in Sec. 2. Next, in Sec. 3, we briefly review the perturbative formula for the SIGW with the primordial scalar non-Gaussianities based on Ref. [34] and provide the predicted signal in relation to current and future experiments. We investigate the detectability for the SIGW with the logarithmic non-Gaussianity in light of PBH DM scenario by the LISA. We also perform the parameter estimation for SIGW in light of the logarithmic non-Gaussianity based on the recent PTA results on the stochastic gravitational wave background, and discuss the compatibility of the abundance of PBHs. Finally, we provide our conclusions in Sec. 4.

2 PBH formation with the logarithmic non-Gaussianity

In this section, we investigate the PBH formation from the primordial curvature perturbation with the logarithmic non-Gaussianity based on peak theory. In general, primordial curvature perturbations can have non-Gaussianities when there is nonlinear evolution. Among several

types of non-Gaussianities, in this work, we focus on a special local-type non-Gaussianity, of which the primordial curvature perturbations ζ can be expressed as a logarithmic function of the Gaussian fluctuations ζ_g as

$$\zeta(\mathbf{x}) = -\frac{1}{\gamma} \ln(1 - \gamma\zeta_g(\mathbf{x})), \quad (2.1)$$

where γ is a parameter that controls the tail behavior of the probability density distribution of the curvature perturbation. Such a logarithmic type of primordial curvature perturbation appears in several inflationary models which can produce PBHs efficiently, *e.g.* [40–45]. The statistical properties of the curvature perturbation differ depending on whether γ is positive or negative. The probability distribution of ζ can be calculated as [42]

$$P(\zeta) = \left| \frac{d\zeta_g}{d\zeta} \right| P_g(\zeta_g(\zeta)) = \frac{1}{\sqrt{2\pi\sigma^2}} \exp \left[-\frac{1}{2\gamma^2\sigma^2} \left(e^{-\gamma\zeta} - 1 \right)^2 - \gamma\zeta \right], \quad (2.2)$$

where $P_g(\zeta_g)$ is the Gaussian distribution and $\sigma^2 = \langle \zeta_g^2 \rangle$ denotes the variance of ζ_g . The tail behavior of the probability density function of ζ is proportional to $\exp(-\gamma\zeta)$ for $\gamma > 0$ and $\exp\left(-\frac{1}{2\gamma^2\sigma^2}e^{-2\gamma\zeta}\right)$ for $\gamma < 0$ respectively.

2.1 Peak profile

The radial profile of the peak of the curvature perturbation $\hat{\zeta}(r)$ is also related to the peak profile of the Gaussian fluctuation $\hat{\zeta}_g(r)$ by the logarithmic mapping [53, 55]

$$\hat{\zeta}(r) = -\frac{1}{\gamma} \ln(1 - \gamma\hat{\zeta}_g(r)). \quad (2.3)$$

We here suppose that the typical peak profile is spherically symmetric about the peak position $\mathbf{x} = \mathbf{0}$ as suggested by the peak theory [56] we will introduce later.¹ The peak profile of a Gaussian field is given by [53, 58, 59],

$$\hat{\zeta}_g(r) = \mu_2 \left[\frac{1}{1 - \gamma_3^2} \left(\psi_1(r) + \frac{1}{3} R_3^2 \Delta \psi_1(r) \right) - \frac{\mu_3^2}{\gamma_3(1 - \gamma_3^2)} \left(\gamma_3^2 \psi_1(r) + \frac{1}{3} R_3^2 \Delta \psi_1(r) \right) \right] + \zeta_g^\infty, \quad (2.4)$$

which is characterized by three parameters: the peak height μ_2 , the width μ_3 , and the overall offset $\zeta_g^\infty (= \hat{\zeta}_g|_{r \rightarrow \infty})$. The statistical quantities and the two-point correlation function are given by

$$\begin{aligned} \sigma_n^2 &= \int \frac{dk}{k} k^{2n} \mathcal{P}_g(k), & \psi_n(r) &= \frac{1}{\sigma_n^2} \int \frac{dk}{k} k^{2n} \frac{\sin(kr)}{kr} \mathcal{P}_g(k), \\ \gamma_n &= \frac{\sigma_n^2}{\sigma_{n-1}\sigma_{n+1}}, & R_n &= \frac{\sqrt{3}\sigma_n}{\sigma_{n+1}}, \quad \text{for odd } n, \end{aligned} \quad (2.5)$$

with ζ_g 's power spectrum

$$\mathcal{P}_g(k) = \frac{k^3}{2\pi^2} \int d^3x e^{-i\mathbf{k}\cdot\mathbf{x}} \left\langle \zeta_g\left(\frac{\mathbf{x}}{2}\right) \zeta_g\left(-\frac{\mathbf{x}}{2}\right) \right\rangle. \quad (2.6)$$

¹See Ref. [57] for the effect of non-sphericity.

We hereafter assume a monochromatic power spectrum for ζ_g , which has a Dirac delta peak at $k = k_*$, as

$$\mathcal{P}_g(k) = A_g \delta(\ln k - \ln k_*) . \quad (2.7)$$

In such a case, the peak profile of Eq. (2.4) reduces to the simpler form (see, e.g., Ref. [53])

$$\hat{\zeta}_g(r) = \mu_2 \psi_1(r) = \mu_2 \frac{\sin(k_* r)}{k_* r} , \quad (2.8)$$

and as a result, the non-Gaussian curvature perturbation reads

$$\hat{\zeta}(r) = -\frac{1}{\gamma} \ln \left(1 - \gamma \mu_2 \frac{\sin(k_* r)}{k_* r} \right) . \quad (2.9)$$

2.2 The Compaction function

In the Friedman–Lemaître–Robertson–Walker (FLRW) universe, the spacetime metric for the spherical symmetric perturbation in the long wavelength limit can be written by

$$ds^2 = -dt^2 + a^2(t) e^{2\zeta(r)} [dr^2 + r^2 d\Omega^2] = -dt^2 + a^2(t) e^{2\zeta(r)} dr^2 + R^2(r) d\Omega^2 , \quad (2.10)$$

where $a(t)$ is the scale factor and the angular line element is $d\Omega^2 = d\theta^2 + \sin^2\theta d\phi^2$ and $R(r) = a e^{\zeta(r)} r$ is the areal radius which relates to the proper size of the overdensity region. It is known that the compaction function is a useful quantity for estimating whether a peak collapses into a black hole or not [60, 61]. In the radiation-dominated universe, the compaction function in terms of the curvature perturbation is given by

$$\mathcal{C}(r) = \frac{2}{3} \left[1 - (1 + r\zeta'(r))^2 \right] . \quad (2.11)$$

The threshold on the maximal compaction function varies for different profiles of the curvature perturbation. However, it was shown that the threshold on the averaged compaction function [62]

$$\bar{\mathcal{C}}_m = \left(4\pi \int_0^{R(r_m)} \mathcal{C}(r) R^2(r) dR(r) \right) / \left(\frac{4\pi}{3} R^3(r_m) \right) , \quad (2.12)$$

is universal, where the radius r_m corresponds to the innermost maximum of $\mathcal{C}(r)$. According to this prescription, when the mean compaction function $\bar{\mathcal{C}}_m$ exceeds the threshold value $\bar{\mathcal{C}}_{\text{th}} = 2/5$, the corresponding peak is supposed to collapse into a PBH [62].

Note that depending on the monotonicity of the areal radius $R(r)$ we define the type I and II fluctuations (see, e.g., a recent paper [63]). The monotonicity of $R(r)$ leads to

$$\frac{dR(r)}{dr} = a e^{\zeta(r)} (1 + r\zeta'(r)) > 0 , \quad (2.13)$$

and the initial curvature perturbation ζ on super-horizon scale is called type I if it satisfies this condition. On the other hand, the areal radius $R(r)$ is no longer monotonic for type II fluctuations.

2.3 The q -function method

It was found that the profile-dependence of the threshold is mainly determined by the second derivative at the maximum of $\mathcal{C}(r)$, which is described by an analytical indicator called “ q -function” in Ref. [62]. In Ref. [64], it was found that the q -function is also very useful in the non-Gaussian case of quadratic expansion with large negative f_{NL} . We will review the q -function method in this subsection.

The metric in terms of the comoving areal radius $\tilde{r}(r) = re^{\zeta(r)} = R(r)/a$ can be written as

$$ds^2 = -dt^2 + a^2(t) \left\{ \frac{d\tilde{r}^2}{1 - K(\tilde{r})\tilde{r}^2} + \tilde{r}^2 d\Omega^2 \right\}. \quad (2.14)$$

The curvature perturbation ζ and the spacial curvature K are related as

$$\zeta(r) = \int_{\infty}^{\tilde{r}(r)} \frac{d\tilde{r}'}{\tilde{r}'} \left(1 - \frac{1}{\sqrt{1 - K(\tilde{r}')\tilde{r}'^2}} \right). \quad (2.15)$$

The compaction function in the comoving coordinate r can be calculated by Eq. (2.11) and the expression in terms of the comoving areal radius \tilde{r} is given by

$$\tilde{\mathcal{C}}(\tilde{r}) = \mathcal{C}(r(\tilde{r})) = \frac{2}{3}K(\tilde{r})\tilde{r}^2. \quad (2.16)$$

If one supposes the following fiducial profile of K characterised by a parameter q , as introduced in Ref. [62],

$$K_q(\tilde{r}) = \frac{3}{2} \frac{\tilde{\mathcal{C}}(\tilde{r}_m)}{\tilde{r}_m^2} \exp \left[\frac{1}{q} \left\{ 1 - \left(\frac{\tilde{r}}{\tilde{r}_m} \right)^{2q} \right\} \right], \quad (2.17)$$

where $\tilde{r}_m = \tilde{r}(r_m)$, the characteristic q parameter (or the q -function, which is an implicit function of the parameters of the peak profile) is related to the maximal compaction and its second derivative:

$$q = -\frac{1}{4} \tilde{r}_m^2 \frac{\tilde{\mathcal{C}}''(\tilde{r}_m)}{\tilde{\mathcal{C}}(\tilde{r}_m)} = -\frac{1}{4} \tilde{r}_m^2 \frac{\mathcal{C}''(r_m)}{\mathcal{C}(r_m)[1 - (3/2)\mathcal{C}(r_m)]}. \quad (2.18)$$

On the other hand, the maximal mean compaction $\bar{\mathcal{C}}_m$ can be analytically calculated for the fiducial profile (2.17) and the criterion $\bar{\mathcal{C}}_m = 2/5$ can be recast into the threshold on the maximal compaction function δ_c as

$$\delta_c = \frac{4}{15} e^{-1/q} \frac{q^{1-5/(2q)}}{\Gamma(5/(2q)) - \Gamma(5/(2q), 1/q)}, \quad (2.19)$$

where $\Gamma(s)$ is the Gamma function and $\Gamma(s, z)$ is the incomplete Gamma function. Interestingly, even for profiles different from the fiducial one (2.17), a simple criterion given by $\mathcal{C}(r_m, q) > \delta_c$ with the q -function calculated by Eq. (2.18) somehow works quite well. Ref. [64] clarified that the corresponding threshold values are consistent with numerical results within 2% errors in the presence of positive or small negative non-Gaussianities, though the discrepancy with respect to the numerical results becomes larger in the presence of large negative f_{NL} for quadratic-expansion non-Gaussianity. We will show that this holds for logarithmic non-Gaussianity too.

2.4 Numerical study on the thresholds

Though the above two analytical criteria work for quadratic-expansion non-Gaussianity with a small f_{NL} , they are not ensured to work for the logarithmic non-Gaussianity. In this work, we hence numerically derive the amplitude threshold ($\mu_{2,c}$) for PBH formation depending on the parameter γ in Eq. (2.1). For this purpose, we use a numerical relativity code based on the Baumgarte–Shapiro–Shibata–Nakamura (BSSN) formalism [65, 66] and reformulated for curvilinear coordinates in spherical symmetry as in Ref. [67]. The matter corresponds to a perfect fluid with a barotropic equation of state, $p = \omega\rho$, where p and ρ are the pressure and energy density of the fluid, respectively, and $\omega = 1/3$ for an ultra-relativistic fluid (radiation). The evolution of the matter components is done by solving the general-relativistic hydrodynamic equations as described in Ref. [68]. See also Ref. [69] for related work on PBH formation. In contrast to alternative codes based on the Misner–Sharp formalism [70–72], we are able to compute the amplitude threshold for PBHs forming from type II fluctuations, where Misner–Sharp codes fail because of the appearance of coordinates singularities. In the parameter region where $\gamma \gtrsim -2$, we have checked and found that both BSSN and Misner–Sharp codes agree, and yield the same results.

Our results for the amplitude threshold for PBH formation across different values for γ is shown with red crosses in Fig. 1. No PBH is formed below this curve. The black solid line denotes the boundary for the type I and type II fluctuations computed by the monotonicity of the areal radius. The parameter space below this line corresponds to type I fluctuations, while type II fluctuations span the parameter space above. The gray solid curve represents the analytical estimation of the threshold evaluated by the q -function method introduced in Sec. 2.3, and the gray dashed curve is obtained from the maximal mean compaction function $\bar{C}_m = 2/5$ shown in Sec. 2.2. The orange curves correspond to the condition where the argument of the logarithmic function in the peak profile Eq. (2.3) equals zero, above which ζ diverges. This implies the inflaton can not evolve classically to end inflation, as the time duration of inflation (described by $\delta\mathcal{N} = \zeta \rightarrow \infty$) in these Hubble patches are infinite. Quantum diffusion must be taken into account the study the fate of such *eternal inflation* regions [73], which have complicated global structure and are beyond the scope of this paper. Near the border of the orange region and the Type II region, such long-lived inflating bubbles will be rare and surrounded by classically evolving spacetime, which also collapse into PBHs finally. Such a bubble channel dominates PBH formation when $\gamma \gtrsim 3.1$ [74], which we will not study in this paper. Therefore we restrict ourselves in $\gamma \lesssim 3.1$. We found that PBHs formed from both type I and type II fluctuations with amplitudes slightly larger than the threshold are classified as so-called type A, a nomenclature introduced in Ref. [63], which corresponds to PBH formed through the gravitational collapse of the overdensity region after the curvature perturbation re-enters the Hubble radius. We expect that type B PBHs introduced in Ref. [63] form only at much larger amplitudes. Then, in terms of the abundance of total PBHs, we consider that the contribution from the type B PBHs would be exponentially suppressed and negligible. Although we do not investigate the details of the formation of the type B PBH, interestingly, contrary to what previously thought, we found a region of type II fluctuations where no black hole is formed, that is, type II fluctuations do not necessarily lead to PBH formation.

2.5 Abundance of PBHs

Based on the result of the threshold for the PBH formation shown above, in this subsection we investigate the abundance of PBHs with logarithmic non-Gaussianity. First of all, we

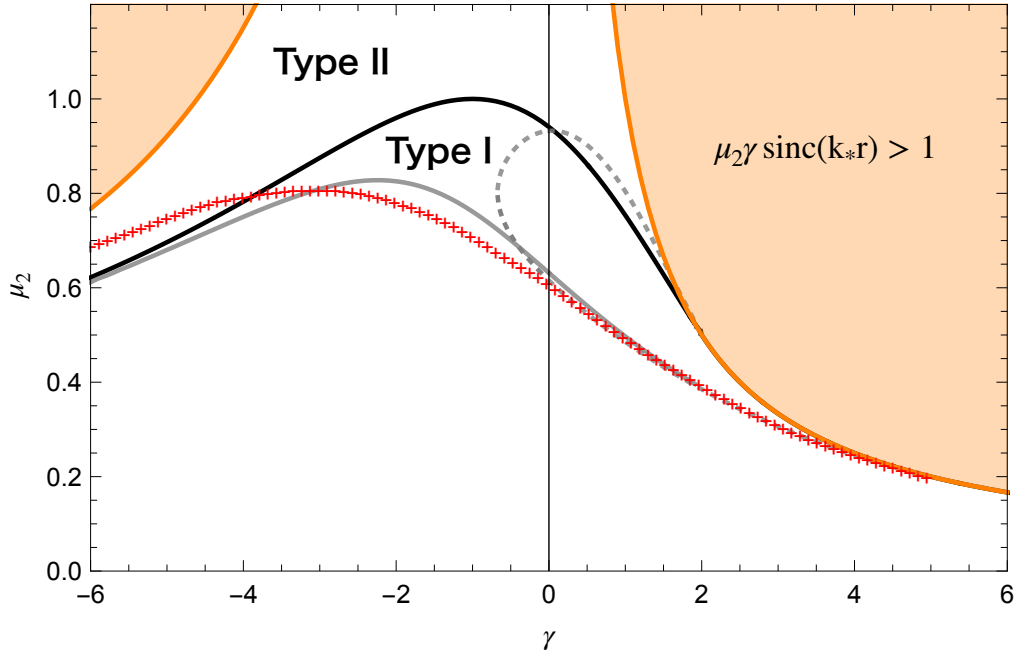


Figure 1: The PBH diagram in terms of the peak amplitude μ_2 in the case of the logarithmic non-Gaussianity. The black solid line denotes the boundary for the type I and type II fluctuations inferred by the monotonicity of the areal radius. The orange lines show the boundary where the inside of the function of Eq. (2.3) coincides with zero. The profile Eq. (2.3) becomes doubtful over the orange lines. The gray curve represents the analytical estimation evaluated by the q -function method. The gray dashed curve corresponds to the maximal mean compaction function $\bar{C}_m = 2/5$. The red cross points denote the thresholds that form type A PBHs obtained by the numerical simulation. The type A PBH formation from the type I fluctuation happens on the red cross points for $-3.8 \lesssim \gamma \lesssim 5.0$. The type A PBH formation from the type II fluctuation occurs on the red cross points in $\gamma \lesssim -3.8$.

suppose that Type A PBHs obey critical collapse, such that the resultant mass follows a scaling relation [75]

$$M_{\text{PBH}} = K(\mu_2 - \mu_{2,c})^p M_H, \quad (2.20)$$

with an universal power $p \simeq 0.36$ [76, 77], an order unity coefficient K , and the threshold $\mu_{2,c}$. For simplicity, we set $K \simeq 1$ in this paper. M_H is the Hubble mass at the Hubble reentry of the maximal radius, $R(r_m)H = 1$. Substituting $R(r_m) = a(t)r_m e^{\zeta(r_m)}$, the PBH mass can be rewritten as

$$M_{\text{PBH}} = K(\mu_2 - \mu_{2,c})^p (k_* r_m)^2 e^{2\zeta(r_m)} M_{k_*}, \quad (2.21)$$

where M_{k_*} is the Hubble mass at the Hubble reentry of the scale k_* in the background universe given by

$$M_{k_*} \simeq 10^{20} \left(\frac{g_*}{106.75} \right)^{-1/6} \left(\frac{k_*}{1.56 \times 10^{13} \text{ Mpc}^{-1}} \right)^{-2} \text{ gram}, \quad (2.22)$$

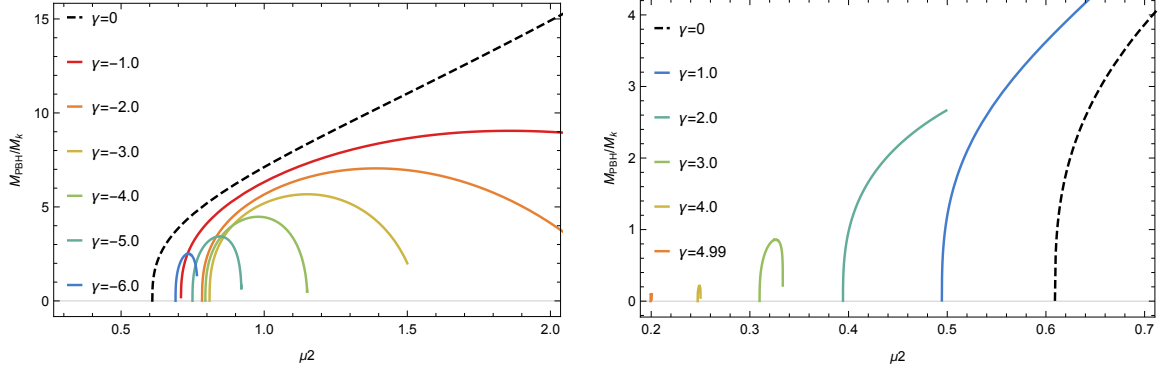


Figure 2: The normalized PBH mass as a function of μ_2 for each value of the negative (left) and the positive (right) γ . Although the PBH has a local maximum for $\gamma < 0$ and $2 < \gamma$, it does not in the range of $0 \leq \gamma \leq 2$.

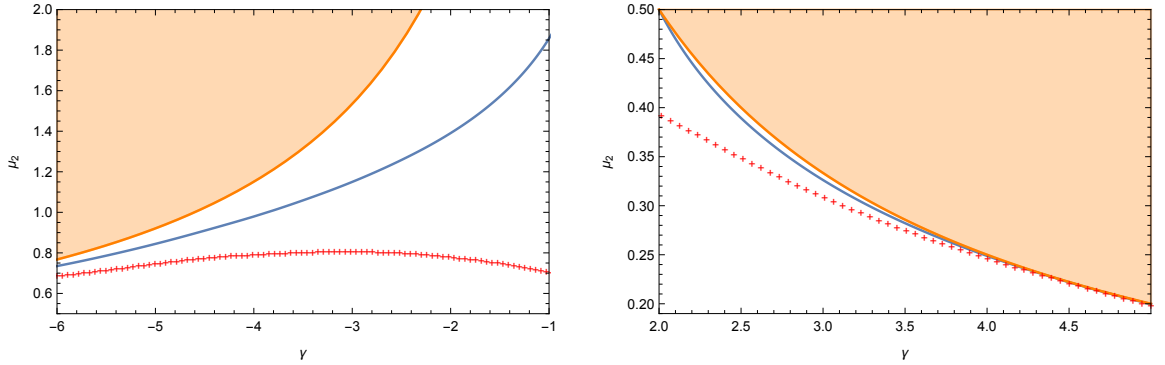


Figure 3: The maximum μ_2 corresponding to the local maximum of PBH mass (blue). The orange shaded areas are the doubtful regions, as in Fig. 1. Red cross points are the numerical threshold, as in Fig. 1.

with the effective degrees of freedom for the energy density g_* at the Hubble crossing. The PBH mass as a function of μ_2 for each γ is exhibited in Fig. 2. While the PBH mass has a local maximum for $\gamma < 0$ and $2 < \gamma$, it does not in the range of $0 \leq \gamma \leq 2$. As we will see later, to evaluate the total abundance of PBHs, we need to perform the integration of the mass function with respect to μ_2 and set a maximum value of μ_2 for each γ . Although we do not know the exact upper bound of μ_2 for the type A PBH formation, we adopt the value of μ_2 which gives the local maximum of PBH mass as the maximum value for $\gamma < 0$ and $2 < \gamma$, which is shown in Fig. 3 as a function of γ by the blue lines. On the other hand, we use $1/\gamma$ (corresponding to the orange line of Fig. 1) as the maximum value of μ_2 for $0 \leq \gamma \leq 2$. We have checked that the total abundance of PBHs is less sensitive to these choices of the maximum value of μ_2 , and this is because the PBH formation mainly happens near the critical threshold $\mu_{2,c}$.

The peak number density with the amplitude μ_2 can be statistically computed by the *peak theory* [56]. Using the relation between μ_2 and the PBH mass in Eq. (2.21), a peak number density can be recast into the current PBH energy density, which is described by the PBH mass function $f_{\text{PBH}}(M)$, defined as the current PBH fraction of the dark matter in the

mass range of $[M, Me^{\text{d ln } M}]$ as²

$$f_{\text{PBH}}(M) \text{d ln } M = \frac{\rho_{\text{PBH},0}}{\rho_{\text{DM},0}} \text{d ln } M \quad (2.23)$$

$$= \left(\frac{\Omega_{\text{DM},0} h^2}{0.12} \right)^{-1} \left(\frac{M}{10^{20} \text{ g}} \right) \left(\frac{k_*}{1.56 \times 10^{13} \text{ Mpc}^{-1}} \right)^3 \left(\frac{\left| \frac{\text{d ln } M}{\text{d} \mu_2} \right|^{-1} f \left(\frac{\mu_2(M)}{\sqrt{A_g}} \right) \mathcal{N}(\mu_2(M), \sqrt{A_g})}{1.4 \times 10^{-14}} \right),$$

where the subscript ‘‘0’’ denotes the value at present, Ω_{DM} is the density parameter of the dark matter, $\mathcal{N}(x, \sigma) = \frac{1}{\sqrt{2\pi}\sigma} \exp\left(-\frac{x^2}{2\sigma^2}\right)$ denotes the zero-mean Gaussian distribution with the variance σ , and the function $f(\xi)$ corresponds to

$$f(\xi) = \frac{1}{2} \xi (\xi^2 - 3) \left(\text{erf} \left[\frac{1}{2} \sqrt{\frac{5}{2}} \xi \right] + \text{erf} \left[\sqrt{\frac{5}{2}} \xi \right] \right) + \sqrt{\frac{2}{5\pi}} \left\{ \left(\frac{8}{5} + \frac{31}{4} \xi^2 \right) \exp \left[-\frac{5}{8} \xi^2 \right] + \left(-\frac{8}{5} + \frac{1}{2} \xi^2 \right) \exp \left[-\frac{5}{2} \xi^2 \right] \right\}. \quad (2.24)$$

The total PBH abundance is obtained by integrating Eq. (2.23)

$$f_{\text{PBH}}^{\text{tot}} = \int f_{\text{PBH}}(M) \text{d ln } M. \quad (2.25)$$

The mass spectrum and the total PBH abundance for the negative and the positive γ are shown in Fig. 4 and Fig. 5 respectively. Though the PBH mass spectrum shows a divergent feature for $\gamma < 0$ and $2 < \gamma$ at the local maximum of the PBH mass due to the Jacobian $\left| \frac{\text{d ln } M}{\text{d} \mu_2} \right|^{-1}$, the total PBH abundance as its integral is convergent thanks to the conservation of the probability. Here, we neglected the contribution from the PBH formation in vacuum bubbles but it should be taken into account numerically for a more precise estimation of the PBH mass spectrum, especially for $\gamma \gtrsim 3.1$ [74]. In this work, we focus solely on type A PBH formation and leave this point for future work.

In Fig. 6, we show the γ dependence of the required amplitude of the Gaussian fluctuations A_g to realize $f_{\text{PBH}}^{\text{tot}} = 1$ for each fixed PBH mass scale $M_{k_*} = 10^{20} \text{ g}$ (blue), and $5.45 \times 10^{28} \text{ g}$ (yellow). As shown in this figure, the required value of A_g decreases for the positive γ since the positive non-Gaussianities promote PBH productions. On the other hand, towards the negative semi-axis of γ , the required A_g increases at first until it reaches its maximum at $\gamma \simeq -3.1$, and then decreases. While a negative non-Gaussianity suppresses the PBH formation between $0 > \gamma \gtrsim -3.1$, somehow counterintuitively, we find that PBH formation again becomes enhanced for larger negative non-Gaussianities below $\gamma \lesssim -3.1$. This trend is because the critical threshold $\mu_{2,c}$ increases as γ decreases, reaches the maximum at $\gamma \simeq -3.1$, and again decreases which is confirmed down to $\gamma = -6.0$. Note that, as we will see later, the mass scales chosen in Fig. 6 correspond to typical frequency of LISA $f_* = 0.023 \text{ Hz}$ and the peak frequency $f_* = 10^{-6} \text{ Hz}$ that is compatible with North American Nanohertz Observatory for Gravitational Waves (NANOGrav) observation when one tries to fit the NANOGrav data with SIGW, respectively. In principle, the value of γ which maximizes A_g depends slightly on

²It should be noted that the PBH abundance expression in the original paper [58] had a factor 1/27 error. It has been corrected in our expression.

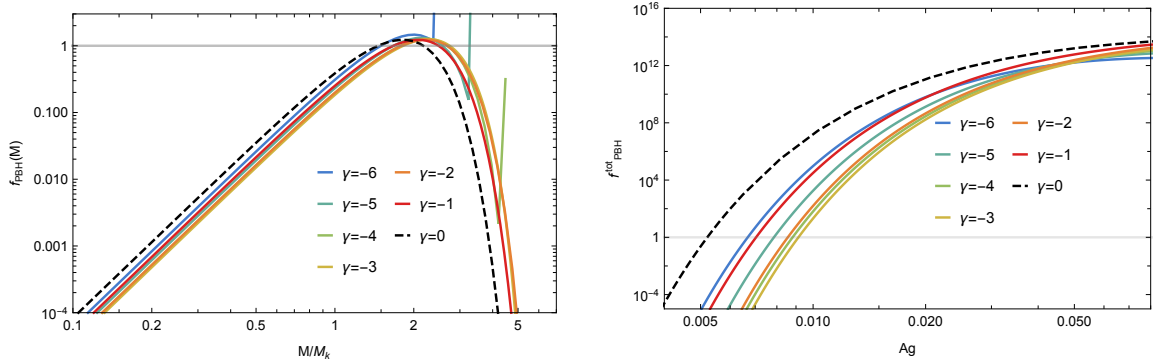


Figure 4: *Left:* the PBH mass spectra for $(A_g, \gamma) = (6.69 \times 10^{-3}, -6)$, $(7.86 \times 10^{-3}, -5)$, $(8.81 \times 10^{-3}, -4)$, $(9.14 \times 10^{-3}, -3)$, $(8.56 \times 10^{-3}, -2)$, $(7.04 \times 10^{-3}, -1)$, and $(5.21 \times 10^{-3}, 0)$ from purple to red and the black dashed line. The amplitude A_g is chosen for each γ so that the total PBH abundance $f_{\text{PBH}}^{\text{tot}}$ becomes unity. *Right:* the total PBH abundance (2.25) for each γ with the same color code as the left panel.

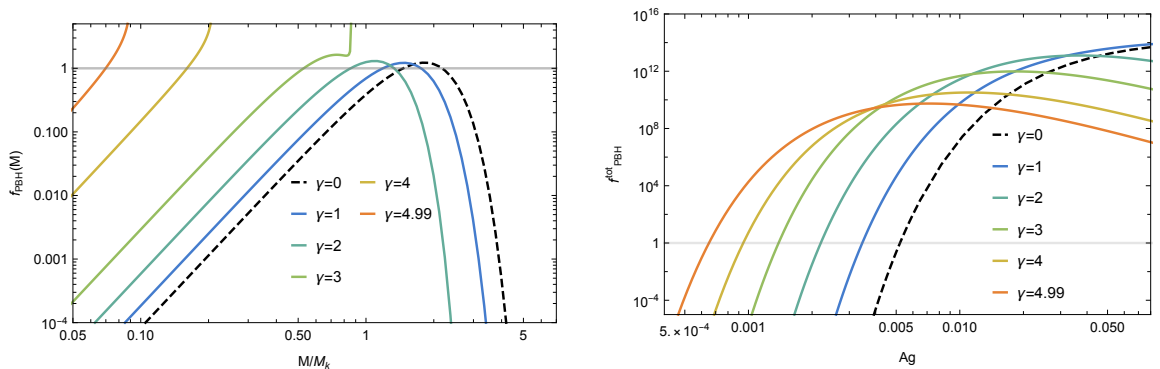


Figure 5: *Left:* the PBH mass spectra for $(A_g, \gamma) = (5.21 \times 10^{-3}, 0)$, $(3.46 \times 10^{-3}, 1)$, $(2.20 \times 10^{-3}, 2)$, $(1.39 \times 10^{-3}, 3)$, $(9.45 \times 10^{-4}, 4)$, and $(6.52 \times 10^{-4}, 4.99)$ by the black dashed line and from blue to yellow. They are again normalized by $f_{\text{PBH}}^{\text{tot}} = 1$. *Right:* the total PBH abundance for the same γ values as the left panel.

the peak frequency which in turn is determined by the mass scale and number of relativistic degrees of freedom at the horizon reentry. We confirmed that its dependence was tiny and takes maximum value at $\gamma \simeq -3.1$ almost irrespective of the peak frequency.

3 The scalar induced gravitational wave signals

3.1 Formulation

We will now briefly review the SIGWs in the presence of primordial non-Gaussianities based on Refs. [33, 34, 78, 79]. The perturbed metric including the gravitational waves can be written as

$$ds^2 = a(\tau)^2 \left[-(1 + 2\Phi(\tau, \mathbf{x})) d\tau^2 + \left((1 - 2\Phi(\tau, \mathbf{x}))\delta_{ij} + \frac{1}{2}h_{ij}(\tau, \mathbf{x}) \right) dx^i dx^j \right], \quad (3.1)$$

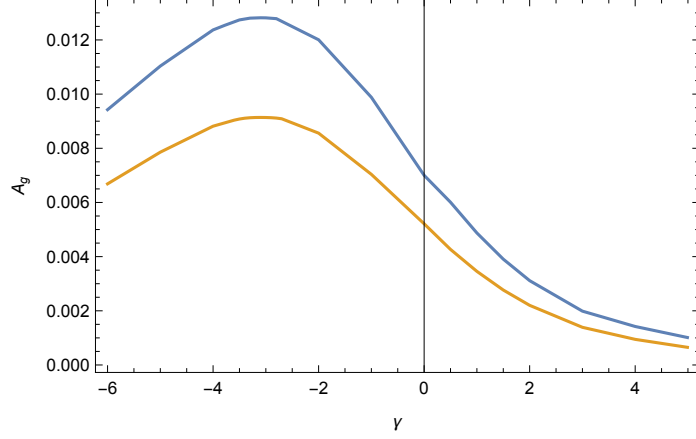


Figure 6: The γ dependence of the required amplitude of the Gaussian fluctuations A_g to realize $f_{\text{PBH}}^{\text{tot}} = 1$ for each fixed PBH mass scale $M_{k_*} = 10^{20}$ g (blue) and 5.45×10^{28} g (yellow). These mass scales correspond to frequencies $f_* = 0.023$ Hz (blue) and 10^{-6} Hz (yellow) respectively.

where τ represents the conformal time, $\Phi(\tau, \mathbf{x})$ is the curvature perturbation in the Newtonian gauge, and $h_{ij}(\tau, \mathbf{x})$ is the transverse traceless tensor perturbation. The tensor perturbation can be expanded by the Fourier modes $h_\lambda(\tau, \mathbf{k})$ as

$$h_{ij}(\tau, \mathbf{x}) = \sum_{\lambda=+, \times} \int \frac{d^3k}{(2\pi)^3} e^{i\mathbf{k}\cdot\mathbf{x}} e_{ij}^\lambda(\mathbf{k}) h_\lambda(\tau, \mathbf{k}), \quad (3.2)$$

where $e_{ij}^\lambda(\mathbf{k})$ denotes the polarization tensors which satisfy the transverse traceless conditions $e_{ij}^\lambda e_{ij}^{\lambda'} = \delta^{\lambda\lambda'}$ and $e_{ii}^\lambda = 0$. The tensor power spectrum $P_{\lambda\lambda'}(\tau, k)$ is defined as

$$\langle h_\lambda(\tau, \mathbf{k}) h_{\lambda'}(\tau, \mathbf{k}') \rangle = (2\pi)^3 \delta^3(\mathbf{k} + \mathbf{k}') P_{\lambda\lambda'}(\tau, k), \quad (3.3)$$

and the dimensionless power spectrum $\mathcal{P}_{\lambda\lambda'}(\tau, k)$ is given by

$$\mathcal{P}_{\lambda\lambda'}(\tau, k) = \frac{k^3}{2\pi^2} P_{\lambda\lambda'}(\tau, k). \quad (3.4)$$

The density parameter per logarithmic wavenumber is given by

$$\Omega_{\text{GW}} = \frac{1}{\rho_{\text{crit}}} \frac{d\rho_{\text{GW}}}{d \log k}, \quad (3.5)$$

where ρ_{crit} and ρ_{GW} are the critical energy density and the energy density of GWs respectively. The energy density parameter of the SIGWs is given by

$$\Omega_{\text{GW}}(\tau, k) = \frac{1}{48} \left(\frac{k}{\mathcal{H}(\tau)} \right)^2 \sum_{\lambda, \lambda'=+, \times} \overline{\mathcal{P}_{\lambda\lambda'}(\tau, k)}, \quad (3.6)$$

where $\mathcal{H} = \partial_\tau \ln a$ is the conformal Hubble parameter and the overline means the oscillation average. We denote a constant GW density parameter in a deep subhorizon limit during the

radiation-dominated (RD) era as $\Omega_{\text{GW}}^{\text{RD}}(k)$, and then the present density parameter can be described as [80]

$$\Omega_{\text{GW}}(\tau_0, k) = \Omega_{\text{r},0} \frac{g^*}{g_0^*} \left(\frac{g_{s,0}^*}{g_s^*} \right)^{4/3} \Omega_{\text{GW}}^{\text{RD}}(k), \quad (3.7)$$

where Ω_{r} is the density parameter of the radiation component, and g^* and g_s^* respectively represent the effective number of relativistic degrees of freedom for the energy and entropy densities. We adopt the standard model values $g^* = g_s^* = 106.75$, $g_0^* = 3.384$, and $g_{s,0}^* = 3.938$.

Up to the first order in tensor and the second order in scalar, the equation of motion (EoM) for the Fourier mode of GWs is given by

$$h_{\lambda}''(\tau, \mathbf{k}) + 2\mathcal{H}(\tau)h_{\lambda}'(\tau, \mathbf{k}) + k^2 h_{\lambda}(\tau, \mathbf{k}) = 4S_{\lambda}(\tau, \mathbf{k}), \quad (3.8)$$

where $S_{\lambda}(\tau, \mathbf{k})$ is the source term quadratic in Φ , and the prime denotes the partial derivative with respect to the conformal time. The source term can be written as

$$S_{\lambda}(\tau, \mathbf{k}) = \int \frac{d^3 q}{(2\pi)^3} Q_{\lambda}(\mathbf{k}, \mathbf{q}) f(|\mathbf{k} - \mathbf{q}|, q, \tau) \zeta(\mathbf{q}) \zeta(\mathbf{k} - \mathbf{q}), \quad (3.9)$$

in terms of the comoving curvature perturbation $\zeta(\mathbf{k})$ with the projection function $Q_{\lambda}(\mathbf{k}, \mathbf{q})$ which reads

$$Q_{\lambda}(\mathbf{k}, \mathbf{q}) = e_{ij}^{\lambda}(\mathbf{k}) q^i q^j = \frac{q^2}{\sqrt{2}} \sin^2 \theta \times \begin{cases} \cos(2\psi) & (\lambda = +), \\ \sin(2\psi) & (\lambda = \times), \end{cases} \quad (3.10)$$

in the spherical coordinate where the GW's propagation direction \mathbf{k} is set as the z -direction. The source factor $f(p, q, \tau)$ in the RD universe is given by

$$f(p, q, \tau) = 3\Phi(p\tau)\Phi(q\tau) + \frac{d\Phi(p\tau)}{d\ln(p\tau)} \frac{d\Phi(q\tau)}{d\ln(q\tau)} + \left(\Phi(p\tau) \frac{d\Phi(q\tau)}{d\ln(q\tau)} + \frac{d\Phi(p\tau)}{d\ln(p\tau)} \Phi(q\tau) \right), \quad (3.11)$$

where $\Phi(x)$ with a single argument is the linear transfer function which relates the primordial curvature perturbation $\zeta(\mathbf{k})$ and the Newton potential $\Phi(\tau, \mathbf{k})$ by

$$\Phi(\tau, \mathbf{k}) = \Phi(k\tau)\zeta(\mathbf{k}), \quad (3.12)$$

with

$$\Phi(x) = -\frac{2}{3} \frac{9}{x^2} \left(\frac{\sin(x/\sqrt{3})}{x/\sqrt{3}} - \cos(x/\sqrt{3}) \right), \quad (3.13)$$

in the RD era. The solution of the EoM can be constructed by the Green function as

$$h_{\lambda}(\tau, \mathbf{k}) = \frac{4}{a(\tau)} \int^{\tau} d\tilde{\tau} G_{\mathbf{k}}(\tau, \tilde{\tau}) a(\tilde{\tau}) S_{\lambda}(\tilde{\tau}, \mathbf{k}), \quad (3.14)$$

where $G_{\mathbf{k}}(\tau, \tilde{\tau}) = \frac{\sin k(\tau - \tilde{\tau})}{k}$ is the tensor Green function. Combining Eq. (3.9) and Eq. (3.14), one finds the two-point function of SIGWs as

$$\begin{aligned} \langle h_{\lambda_1}(\tau, \mathbf{k}_1) h_{\lambda_2}(\tau, \mathbf{k}_2) \rangle &= \int \frac{d^3 q_1}{(2\pi)^3} \int \frac{d^3 q_2}{(2\pi)^3} Q_{\lambda_1}(\mathbf{k}_1, \mathbf{q}_1) Q_{\lambda_2}(\mathbf{k}_2, \mathbf{q}_2) \\ &\times I_k(|\mathbf{k}_1 - \mathbf{q}_1|, q_1, \tau) I_k(|\mathbf{k}_2 - \mathbf{q}_2|, q_2, \tau) \langle \zeta(\mathbf{q}_1) \zeta(\mathbf{k}_1 - \mathbf{q}_1) \zeta(\mathbf{q}_2) \zeta(\mathbf{k}_2 - \mathbf{q}_2) \rangle, \end{aligned} \quad (3.15)$$

with the kernel function

$$I_k(p, q, \tau) = 4 \int^{\tau} d\tilde{\tau} G_{\mathbf{k}}(\tau, \tilde{\tau}) \frac{a(\tilde{\tau})}{a(\tau)} f(p, q, \tilde{\tau}). \quad (3.16)$$

Based on the previous works [33, 34], by introducing the perturbative description of the local type non-Gaussianity as

$$\zeta(\mathbf{x}) = \zeta_g(\mathbf{x}) + F_{\text{NL}}\zeta_g^2(\mathbf{x}) + G_{\text{NL}}\zeta_g^3(\mathbf{x}) + H_{\text{NL}}\zeta_g^4(\mathbf{x}) + I_{\text{NL}}\zeta_g^5(\mathbf{x}) + \dots, \quad (3.17)$$

with the non-linearity parameters F_{NL} , G_{NL} , H_{NL} , I_{NL} , etc., we can perturbatively evaluate the SIGWs in the presence of the primordial non-Gaussianity. In the case of the logarithmic non-Gaussianity parameterized by γ , the perturbative non-linear parameters are respectively given as $F_{\text{NL}} = \gamma/2$, $G_{\text{NL}} = \gamma^2/3$, $H_{\text{NL}} = \gamma^3/4$, $I_{\text{NL}} = \gamma^4/5$, and so on. Substituting Eq. (3.17) into Eq. (3.15) and assuming the monochromatic power spectrum for the Gaussian fluctuations (2.7), one can obtain non-Gaussian corrections against the energy density of the GWs order by order of A_g . The total amplitude of the energy density parameter Ω_{GW} is determined by the combination of the non-linearity parameters and the amplitude of the Gaussian fluctuations, for example, it contains terms proportional to A_g^2 , $F_{\text{NL}}^2 A_g^3$, $(F_{\text{NL}} A_g)^4$, and so on. For details of the calculations, see Ref. [34].

3.2 SIGW associated with PBH dark matter

The resultant SIGW signals for the logarithmic non-Gaussianity are shown in Fig. 7 and Fig. 8, supposing monochromatic Gaussian fluctuations which have a peak at $k_* = 1.56 \times 10^{13} \text{ Mpc}^{-1}$ corresponding to $M_{k_*} = 10^{20} \text{ g}$ compatible with the PBH DM scenario. The signals are compared with the LISA sensitivity. For the positive γ shown in Fig. 8, the required SIGW amplitude to realize $f_{\text{PBH}}^{\text{tot}} = 1$ is suppressed as γ becomes larger since the positive non-Gaussianity promotes PBH productions, requiring less typical amplitude of the curvature perturbations. As in Appendix A, the spectrum of SIGW is well converged and higher order corrections are subdominant for the positive γ . Although the amplitude is attenuated, the SIGW signals compatible with the PBH DM are large enough to be detectable in the LISA sensitivity. For the negative γ in Fig. 7, the SIGW signals in the PBH DM scenario increases as γ is smaller for $-3 \lesssim \gamma < 0$, and they would be detectable in LISA. This behavior is similar to that of the required amplitude of the Gaussian fluctuations A_g shown in Fig. 6. For the case with $\gamma \lesssim -3$, the SIGW signals appear to be saturated for the changes in γ around $-5 \lesssim \gamma \lesssim -4$. However, we found that we have to be concerned about the validity of the perturbative calculation for the SIGW. As discussed in Appendix A, while the higher-order collections in the SIGW spectra are well converged for $-4 \lesssim \gamma \leq 0$, the perturbative calculation has failed due to relatively large non-Gaussianity for $\gamma \lesssim -4$. In this regime, some non-perturbative schemes should be required to accurately compute the SIGW, though they are beyond the scope of this paper.

3.3 SIGW in light of recent PTA results

We also discuss the compatibility of the recent reports about the nHz stochastic gravitational wave background (SGWB) by the PTA experiments (the NANOGrav 15-year data in particular) [16–19] with SIGWs in light of the logarithmic non-Gaussianity. We have performed the parameter estimation against our model with the public Python module PTArcade [82]. We consider contributions up to A_g^3 and include the term proportional to G_{NL} which was

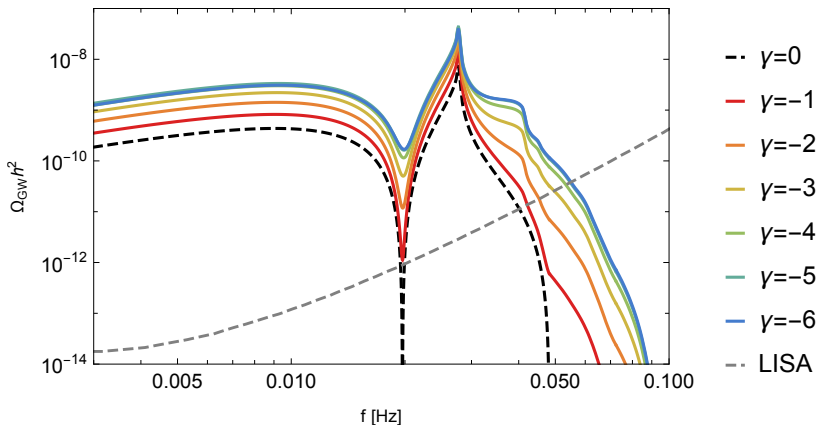


Figure 7: The SIGW spectrum for each γ value up to $\mathcal{O}(A_g^4)$ as in Ref. [34]. We assume a Dirac-delta power spectrum for the Gaussian fluctuations on $k_*/\text{Mpc}^{-1} = 1.56 \times 10^{13}$ corresponding to $M_{k_*} = 10^{20}$ g. The gray dashed line represents the LISA sensitivity curve assuming one-year observation [81]. We used reference values $(A_g, \gamma) = (6.69 \times 10^{-3}, -6)$, $(7.86 \times 10^{-3}, -5)$, $(8.81 \times 10^{-3}, -4)$, $(9.14 \times 10^{-3}, -3)$, $(8.56 \times 10^{-3}, -2)$, $(7.04 \times 10^{-3}, -1)$, and $(5.21 \times 10^{-3}, 0)$ for the plots so that $f_{\text{PBH}}^{\text{tot}} = 1$.

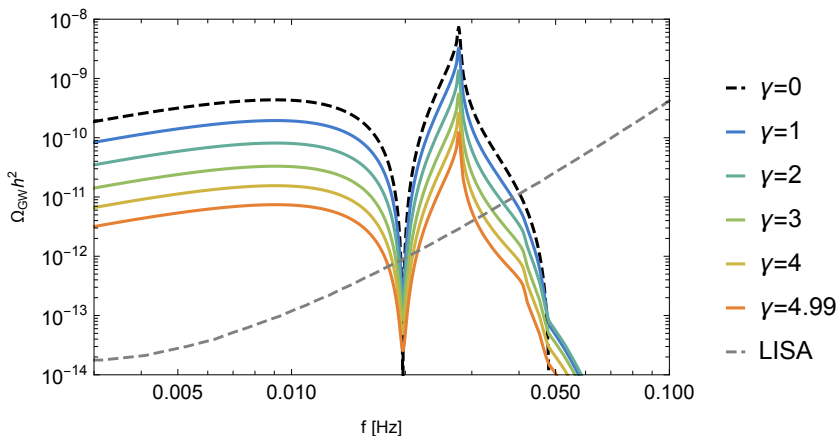


Figure 8: The same plot as Fig. 7 but for positive γ 's. We used reference values $(A_g, \gamma) = (5.21 \times 10^{-3}, 0)$, $(3.46 \times 10^{-3}, 1)$, $(2.20 \times 10^{-3}, 2)$, $(1.39 \times 10^{-3}, 3)$, $(9.45 \times 10^{-4}, 4)$, and $(6.52 \times 10^{-4}, 4.99)$.

not contained in the previous analysis [83]. Our prior choice is displayed in Table 1 and the resultant posterior plot is shown in Fig. 9. The color curves represent the γ dependence of the required A_g to realize $f_{\text{PBH}}^{\text{tot}} = 1$ for each reference peak frequency $f_*/\text{Hz} = 10^{-8}$ (green), 10^{-7} (orange), and 10^{-6} (blue). The PBH overproduction happens if A_g is larger than these lines. We used the scale and the peak frequency relation which is given by

$$f_* = 10^{-9} \left(\frac{k_*}{6.68 \times 10^5 \text{ Mpc}^{-1}} \right) \text{ Hz}. \quad (3.18)$$

The gray-shaded regions represent the limitations of our analysis. In the upper shaded region ($\gamma \gtrsim 3.1$), the PBHs formed in the bubble channel become dominant [74], which are completely

Parameters	Prior
$\log_{10} A_g$	LogUniform $[-4, 1]$
$\log_{10} f_*/[\text{Hz}]$	LogUniform $[-8, -6]$
γ	Uniform $[-6.0, 4.99]$

Table 1: Prior distributions used for the parameter estimation. f_* is the peak frequency of the primordial scalar power spectrum which is chosen within the suitable frequency range for NANOGrav observation.

neglected in our calculation. Carefully taking such PBHs into account will drive all the colored curves in this region to the left, and make it even more difficult to fit the data. On the other hand, in the lower shaded region ($\gamma \lesssim -4$), the high-order terms contributes more to the SIGW, thus our calculation up to $\mathcal{O}(A_g^3)$ underestimates Ω_{GW} . The posterior A_g contour after considering all higher-order contributions might move to the left, yet we do not have a satisfying method to calculate them systematically. Nevertheless, such a trend implies that it might be possible to interpret nHz SGWB as the SIGW in the logarithmic non-Gaussianity with large and negative $\gamma \lesssim -4$. However, one of the main results of our paper is that such an interpretation inevitably have the PBH overproduction problem when $\gamma \gtrsim -4$. This is clearly shown by the black solid line in Fig. 6, which corresponds to $f_{\text{PBH}}^{\text{tot}} = 1$ for $\gamma = -3.1$ where the required amplitude A_g becomes maximum for the changes in γ . PBHs are overproduced even in this case, as the $2\text{-}\sigma$ contour of the posterior A_g is still above this line, and such tension is more serious for other values of γ , as long as $\gamma \gtrsim -4$. Note that our result supposes that all observed SGWB are caused by SIGWs and the result can be milder if one allows other possible sources such as the super massive black hole mergers (e.g., see Fig. 7 in Ref. [16]).

4 Conclusions

In this paper, we have investigated the PBH formation and the associated SIGW signals with the logarithmic non-Gaussianity which is motivated in a wide class of inflation models. By using the numerical relativistic simulation, we first investigated the threshold for the type A PBH formation with respect to the peak height μ_2 and the parameter γ which characterizes the non-Gaussian property of the primordial perturbation. Our results for the threshold for PBH formation across different values for γ are shown with red cross points in Fig. 1. We have found that PBHs formed from both type I and type II fluctuations with amplitudes slightly larger than the threshold are classified as so-called type A, a nomenclature introduced in Ref. [63]. We also found a region where no PBH is formed from type II fluctuations contrary to the previous thought and concluded that type II fluctuation is not necessarily accompanied by PBH formation.

By using the resultant threshold depending on the non-linearity parameter γ , we have calculated the PBH mass spectrum and the total PBH abundance. Our results for the negative and the positive γ are shown in Fig. 4 and Fig. 5 respectively. Though the PBH mass spectrum shows a divergent feature for $\gamma < 0$ and $2 < \gamma$ at the local maximum of the PBH mass due to the Jacobian $\left| \frac{d \ln M}{d \mu_2} \right|^{-1}$, the total PBH abundance as its integral is convergent thanks to the conservation of the probability. Although we neglected the contribution from the PBH formation in vacuum bubbles, it is needed to take into account numerically for a more precise estimation of the PBH mass spectrum in $\gamma \gtrsim 3.1$ [74]. In this work, we focus solely on

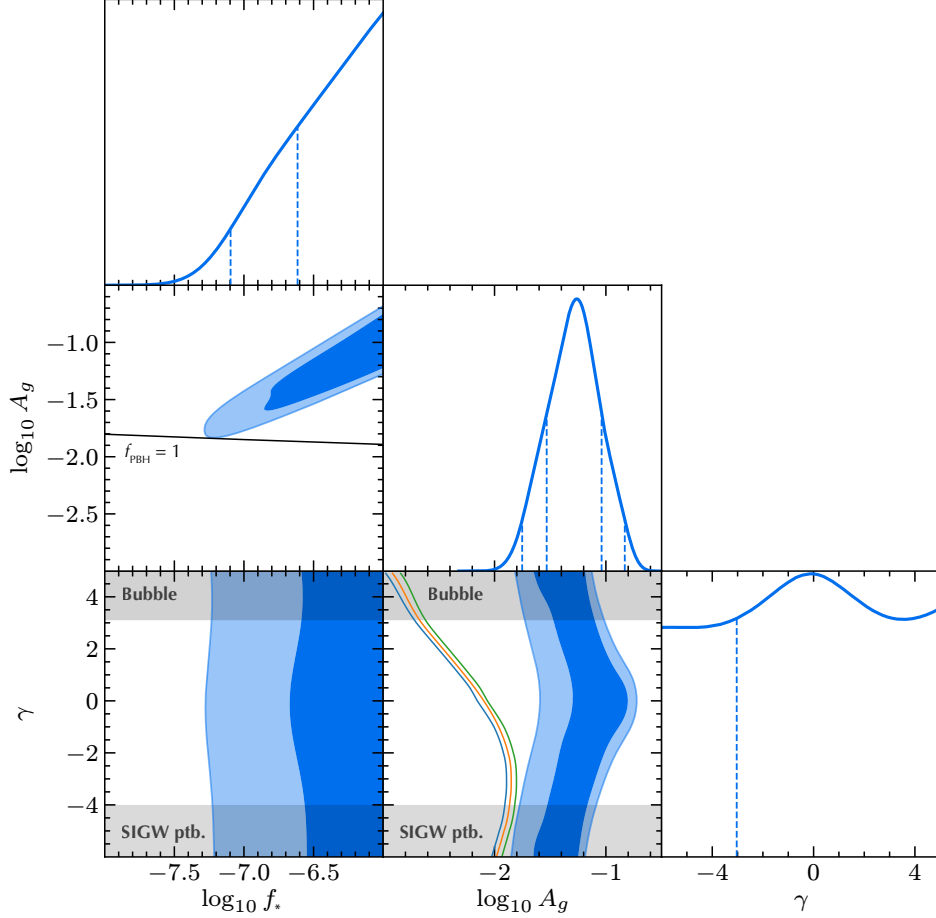


Figure 9: The posterior plot generated by the NANOGrav result. For SIGWs, we include contributions up to $\mathcal{O}(A_g^3)$. The black solid line in the A_g - f_* figure denotes $f_{\text{PBH}}^{\text{tot}} = 1$ for $\gamma = -3.1$, above which the PBHs are overproduced. The color curved in γ - A_g figure also represent $f_{\text{PBH}}^{\text{tot}} = 1$ with fixed $f_*/\text{Hz} = 10^{-8}$ (green), 10^{-7} (orange), and 10^{-6} (blue). The gray-shaded regions represent doubtful regimes where the PBH formations from vacuum bubbles are dominated ($\gamma \gtrsim 3.1$) or the perturbative computation of SIGWs fails ($\gamma \lesssim -4$). We used the public code PTArcade [82] for the plot.

type A PBH formation and leave this point for future work. The required amplitude A_g to realize $f_{\text{PBH}}^{\text{tot}} = 1$, that is, in PBH DM scenario, for each fixed PBH mass scale is shown in Fig. 6. The value of A_g decreases for the positive γ when the total PBH abundance is fixed in unity since the positive non-Gaussianities promote PBH productions. On the other hand, A_g value increases for the negative γ , takes maximum at $\gamma \simeq -3.1$, and decreases again at least down to $\gamma = -6.0$. While the negative non-Gaussianities suppress the PBH formations for $0 > \gamma \gtrsim -3.1$, counterintuitively, the enhancement of PBH formations happens for $\gamma \lesssim -3.1$. This feature comes from the similar tendency of the threshold as shown in Fig. 1.

We have also computed the SIGW signals in PBH DM scenario, that is, $f_{\text{PBH}}^{\text{tot}} = 1$. The resultant SIGW signals with the logarithmic non-Gaussianity are shown in Fig. 7 and Fig. 8, supposing monochromatic Gaussian curvature perturbations on $k_* = 1.56 \times 10^{13} \text{ Mpc}^{-1}$ corresponding to $M_{k_*} = 10^{20} \text{ g}$ compatible with the PBH DM scenario. In the positive γ region,

the SIGW amplitude corresponding to $f_{\text{PBH}}^{\text{tot}} = 1$ is suppressed as γ becomes larger since the positive non-Gaussianity promotes PBH productions, requiring less scalar perturbations. In the calculation of SIGWs, we employ the perturbative approach discussed in Ref. [34], confirming that the SIGW spectra are well converged and higher order corrections are subdominant for the positive γ . Although the amplitude is attenuated, the SIGW signals are large enough to be detectable in the LISA sensitivity. For negative γ case, the required scalar perturbation is larger, which predicts higher SIGW than the Gaussian case, easier to be detected by LISA. However, we found that we have to be concerned about the validity of the perturbative calculation for the SIGW. While the higher-order contributions to the SIGW spectra are well converged for $-4 \lesssim \gamma \leq 0$, the perturbative calculation has failed due to the existence of relatively large non-Gaussianity for $\gamma \lesssim -4$. Non-perturbative schemes are required to accurately compute the SIGW in this regime.

Finally, we discussed the possibility of explaining the SGWB signal reported by the recent PTA experiments by the SIGWs with the logarithmic non-Gaussianity. The resultant posterior plot for the model parameters is exhibited in Fig. 9. Although there are suitable parameter regions consistent with the NANOGrav data, PBH overproduction is a serious problem. However, it is implied that higher-order contributions when $\gamma \lesssim -4$ might alleviate the tension, yet the non-perturbative schemes to calculate the SIGW is necessary to study this problem quantitatively.

Note added: At the stage where our results are being compiled into this paper, we noticed that Masaaki Shimada, Albert Escrivà, Daiki Saito, Koichiro Uehara, and Chul-Moon Yoo were working on similar issues. The works of our groups were conducted independently, and we agreed to submit our paper to arXiv on the same day.

Acknowledgments

We thank the authors of Ref. [84] for discussions on the type B PBH formation scenario. We also thank Jaume Garriga and Richard Bond for useful comments. This work is supported in part by the National Key Research and Development Program of China Grant No. 2020YFC2201502 (SP), and by JSPS KAKENHI Grants No. JP22K03639 (HM), JP24K00624 (SP), JP24K07047 (YT), JP20K03968 (SY), JP24K00627 (SY), and JP23H00108 (SY). RI is supported by JST SPRING, Grant No. JPMJSP2125, and the “Interdisciplinary Frontier Next-Generation Researcher Program of the Tokai Higher Education and Research System”. CJ is funded by the National Natural Science Foundation of China (NSFC) grant No. 12347132, and NSFC RFIS grant No. W2433007. SP is supported by NSFC grant No. 12475066 and No. 12047503. SP and SY are also supported by the World Premier International Research Center Initiative (WPI Initiative), MEXT, Japan.

A The convergence of the scalar-induced gravitational waves

In this section, we discuss the convergence of the perturbative calculation of SIGWs for the negative and positive γ . The contribution at each order (blue for $\mathcal{O}(A_g^2)$, yellow dashed for $\mathcal{O}(A_g^3)$, and green dashed for $\mathcal{O}(A_g^4)$) for the negative and positive γ is shown in Fig. 10 and Fig. 11. In the negative γ region, while the GW spectra are well converged for $-4 \lesssim \gamma \leq 0$, the non-Gaussian collections dominate over the leading term in $\gamma \lesssim -4$. Although the perturbative expansion failed for $\gamma \lesssim -4$, we can safely compute the maximum GW spectrum

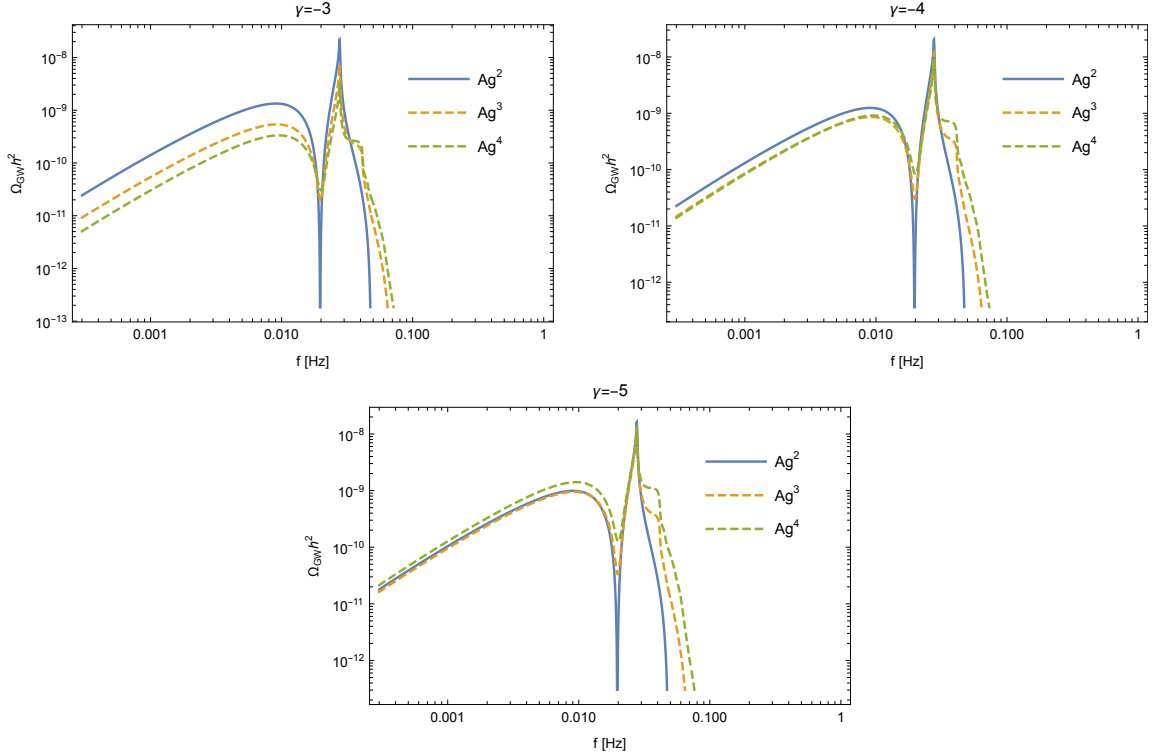


Figure 10: The SIGW plots for $\gamma = -3$ (top left), $\gamma = -4$ (top right), and $\gamma = -5$ (bottom). The blue lines show the contribution order of $\mathcal{O}(A_g^2)$, the yellow dashed lines for $\mathcal{O}(A_g^3)$, and the green dashed lines for $\mathcal{O}(A_g^4)$.

around $\gamma = -3.1$ which corresponds to the maximum value of A_g in our model. On the other hand, in the positive γ region, the GW spectra are well converged and one can safely neglect higher-order corrections.

B The BSSN formalism of Numerical Relativity

In all generality, the line element in the $3 + 1$ dimension reads

$$ds^2 = -\alpha^2 dt^2 + \gamma_{ij}(dx^i + \beta^i dt)(dx^j + \beta^j dt) \quad (\text{B.1})$$

where γ_{ij} is the metric of the 3-dimensional hypersurface, and the lapse and shift gauge parameters are given by α and β^i respectively. We follow with the conventional conformal decomposition of the 3-metric, $\gamma_{ij} = \psi^4 \tilde{\gamma}_{ij}$ where ψ is the conformal factor. The extrinsic curvature K_{ij} is split into its conformal traceless part \tilde{A}_{ij} and trace K ,

$$K_{ij} = \frac{1}{\chi} \left(\tilde{A}_{ij} + \frac{1}{3} \tilde{\gamma}_{ij} K \right). \quad (\text{B.2})$$

For numerical stability, the first spatial derivatives of the metric $\hat{\Delta}^i \equiv -\partial_j \tilde{\gamma}^{ij}$ are considered as dynamical variables.

In spherical symmetric configurations, the spatial metric element reduces to

$$dl^2 = e^{4\chi(r,t)} (a(r,t) dr^2 + r^2 b(r,t) d\Omega^2), \quad (\text{B.3})$$

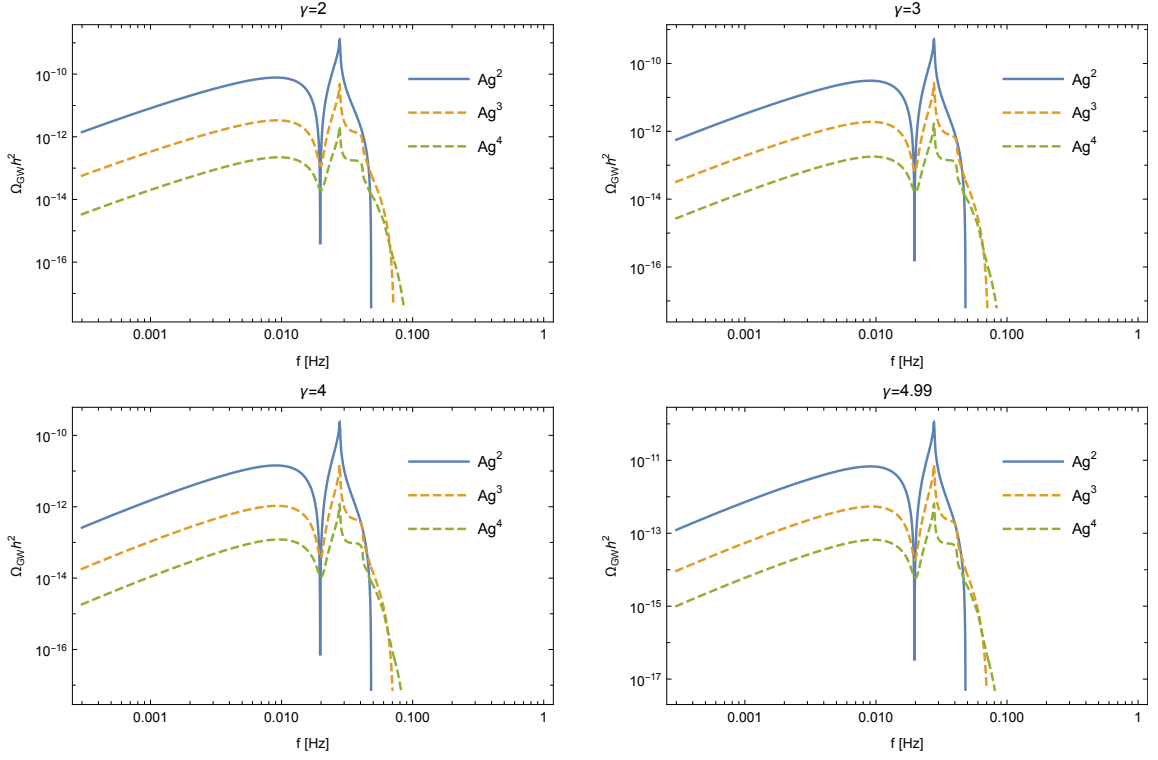


Figure 11: The same plots as Fig. 10 but for $\gamma = 2$ (top left), $\gamma = 3$ (top right), $\gamma = 4$ (bottom left), and $\gamma = 4.99$ (bottom right).

where $a(r, t) \equiv \tilde{\gamma}_{rr}$ and $b(r, t) \equiv \tilde{\gamma}_{\theta\theta}/r$ are coefficients related to the conformal metric, and $\chi(r, t)$ is a redefinition of the conformal factor. We also redefine traceless extrinsic curvature using mixed component $A_a \equiv \gamma^{rr} A_{rr}$ and $A_b \equiv \gamma^{\theta\theta} A_{\theta\theta} = \gamma^{\phi\phi} A_{\phi\phi}$, where naturally the relation $A_a = -2A_b$ holds.

The evolution equations of the BSSN dynamical variables are then given by

$$\partial_t \chi = \beta^r \partial_r \chi - \frac{1}{6} \alpha K, \quad (\text{B.4})$$

$$\partial_t a = \beta^r \partial_r a + 2a \partial_r \beta^r - 2\alpha a A_a, \quad (\text{B.5})$$

$$\partial_t b = \beta^r \partial_r b + 2b \frac{\beta^r}{r} - 2\alpha b A_b. \quad (\text{B.6})$$

$$\begin{aligned} \partial_t K &= \beta^r \partial_r K - \nabla^2 \alpha + \alpha \left(A_a^2 + 2A_b^2 + \frac{1}{3} K^2 \right) \\ &\quad + 4\pi \alpha (\rho + S_a + 2S_b), \end{aligned} \quad (\text{B.7})$$

$$\begin{aligned} \partial_t A_a &= \beta^r \partial_r A_a - \left(\nabla^r \nabla_r \alpha - \frac{1}{3} \nabla^2 \alpha \right) + \alpha \left(R_r^r - \frac{1}{3} R \right) \\ &\quad + \alpha K A_a - \frac{16}{3} \pi \alpha (S_a - S_b), \end{aligned} \quad (\text{B.8})$$

$$\begin{aligned} \partial_t \hat{\Delta}^r &= \beta^r \partial_r \hat{\Delta}^r - \hat{\Delta}^r \partial_r \beta^r + \frac{1}{a} \partial_r^2 \beta^r + \frac{2}{b} \partial_r \left(\frac{\beta^r}{r} \right) \\ &\quad - \frac{2}{a} (A_a \partial_r \alpha + \alpha \partial_r A_a) + 2\alpha \left(A_a \hat{\Delta}^r - \frac{2}{rb} (A_a - A_b) \right) \\ &\quad + \frac{2\alpha}{a} \left[\partial_r A_a - \frac{2}{3} \partial_r K + 6A_a \partial_r \chi + (A_a - A_b) \left(\frac{2}{r} + \frac{\partial_r b}{b} \right) - 8\pi S_r \right], \end{aligned} \quad (\text{B.9})$$

where ρ and S_r are, respectively, the total energy density and the covariant component of the momentum density which are defined below. Note that the system of equations respects covariance, only that the terms of $\tilde{\gamma}^{rr} = a^{-1}$ and $\tilde{\gamma}^{\theta\theta} = \tilde{\gamma}^{\phi\phi} = 1/(br^2)$ have been explicitly written. The covariant derivatives with respect to the four-metric for the lapse function are computed as follows

$$\nabla^2 \alpha = \frac{1}{ae^{4\chi}} \left[\partial_r^2 \alpha - \partial_r \alpha \left(\frac{\partial_r a}{2a} - \frac{\partial_r b}{b} - 2\partial_r \chi - \frac{2}{r} \right) \right], \quad (\text{B.10})$$

$$\nabla^r \nabla_r \alpha = \frac{1}{ae^{4\chi}} \left[\partial_r^2 \alpha - \partial_r \alpha \left(\frac{\partial_r a}{2a} + 2\partial_r \chi \right) \right]. \quad (\text{B.11})$$

And the components of the Ricci tensor and Ricci scalar, in spherical symmetry, are given by

$$\begin{aligned} R_r^r &= -\frac{1}{ae^{4\chi}} \left[\frac{\partial_r^2 a}{2a} - a \partial_r \hat{\Delta}^r - \frac{3}{4} \left(\frac{\partial_r a}{a} \right)^2 + \frac{1}{2} \left(\frac{\partial_r b}{b} \right)^2 - \frac{1}{2} \hat{\Delta}^r \partial_r a + \frac{\partial_r a}{rb} \right. \\ &\quad \left. + \frac{2}{r^2} \left(1 - \frac{a}{b} \right) \left(1 + \frac{r \partial_r b}{b} \right) + 4 \partial_r^2 \chi - 2\partial_r \chi \left(\frac{\partial_r a}{a} - \frac{\partial_r b}{b} - \frac{2}{r} \right) \right], \end{aligned} \quad (\text{B.12})$$

$$\begin{aligned} R &= -\frac{1}{ae^{4\chi}} \left[\frac{\partial_r^2 a}{2a} + \frac{\partial_r^2 b}{b} - a \partial_r \hat{\Delta}^r - \left(\frac{\partial_r a}{a} \right)^2 + \frac{1}{2} \left(\frac{\partial_r b}{b} \right)^2 + \frac{2}{rb} \left(3 - \frac{a}{b} \right) \partial_r b \right. \\ &\quad \left. + \frac{4}{r^2} \left(1 - \frac{a}{b} \right) + 8 (\partial_r^2 \chi + (\partial_r \chi)^2) - 8\partial_r \chi \left(\frac{\partial_r a}{2a} - \frac{\partial_r b}{b} - \frac{2}{r} \right) \right]. \end{aligned} \quad (\text{B.13})$$

B.1 Gravitational hydrodynamics

We consider cosmological settings in the radiation domination epoch where assume the energy-momentum tensor of the perfect fluid,

$$T_{\mu\nu} = (\rho_{\text{fl}} + p) u_\mu u_\nu + p g_{\mu\nu}, \quad (\text{B.14})$$

where ρ_{fl} and p are the fluid's energy density and pressure, respectively, and u_μ is the four-velocity. We use a barotropic equation of state, with $p = \omega\rho_{\text{fl}}$ and fix $\omega = 1/3$ according to a radiation fluid. From a comoving observer, the fluid's energy density is commonly described by splitting it into the rest energy density ρ_0 and the internal energy ε , such that $\rho_{\text{fl}} \equiv \rho_0(1 + \varepsilon)$. In such a way, for an ideal fluid corresponding to the ultra-relativistic matter (i.e. radiation), we have $\varepsilon \gg 1$, and so $\rho_{\text{fl}} \simeq \rho_0\varepsilon$. For an Eulerian observer, the total energy density ρ is then given by

$$\rho = (\rho_{\text{fl}} + p)W^2 - p , \quad (\text{B.15})$$

where $W \equiv 1/\sqrt{1 - v^2}$ is the Lorentz factor, with v^i being the three-velocity component of the fluid as seen by the Eulerian observer.

The state of the fluid is described at any time by the *primitive variables* ρ_0 , ε , p , and v^i . The evolution equations of such a system can be derived from the conservation laws

$$\nabla_\mu (\rho_0 u^\mu) = \partial_\mu (\sqrt{-g} \rho_0 u^\mu) = 0 , \quad (\text{B.16})$$

and

$$\nabla_\mu T_\nu^\mu = \partial_\mu (\sqrt{-g} T_\nu^\mu) - \sqrt{-g} \Gamma_{\mu\nu}^\alpha T_\alpha^\mu = 0 . \quad (\text{B.17})$$

In here, we skip the full derivation of the equations of motion as these can be found in full detail in Ref. [68]. The procedure leads to a system of equations where a new set of variables is defined to be used during the evolution. These are the *conserved variables* D , S_i and \mathcal{E} , and they are defined in terms of the primitive variables, such that

$$D \equiv \rho_0 W , \quad (\text{B.18})$$

$$S_i \equiv (\rho_{\text{fl}} + p)W^2 v_i , \quad (\text{B.19})$$

$$\mathcal{E} \equiv (\rho_{\text{fl}} + p)W^2 - p - D . \quad (\text{B.20})$$

The evolution equation for the fluid, written in terms of BSSN variables, is then given by

$$(\partial_t - \mathcal{L}_\beta) D = -D_k (\alpha D v^k) + \alpha K D , \quad (\text{B.21})$$

$$\begin{aligned} (\partial_t - \mathcal{L}_\beta) S^i &= -D_k \left[\alpha \left(S^i v^k + \gamma^{ik} p \right) \right] \\ &\quad - (\mathcal{E} + D) D^i \alpha + \alpha K S^i , \end{aligned} \quad (\text{B.22})$$

$$\begin{aligned} (\partial_t - \mathcal{L}_\beta) \mathcal{E} &= (\mathcal{E} + D + p) (\alpha v^m v^n K_{mn} - v^m \partial_m \alpha) \\ &\quad - D_k \left[\alpha v^k (\mathcal{E} + D) \right] + \alpha K (\mathcal{E} + p) , \end{aligned} \quad (\text{B.23})$$

where D_i denotes the covariant derivative with respect to the spatial metric. A generic equation of state often requires a root-finding technique to obtain the value of p and v^i , prior to the recovery of the other variables, as they are needed to evolve Eqs. (B.21)–(B.23). However, for cases with a simple equation of state, the recovery of p and v^i can be done analytically by finding the physical root of a high-order polynomial. For a barotropic fluid with $p = \omega\rho_{\text{fl}}$, this implies solving a second-order polynomial [69], which diminishes the computational burden of the simulations.

References

- [1] S. Hawking, *Gravitationally collapsed objects of very low mass*, *Mon. Not. Roy. Astron. Soc.* **152** (1971) 75.

- [2] B. J. Carr and S. W. Hawking, *Black holes in the early Universe*, *Mon. Not. Roy. Astron. Soc.* **168** (1974) 399.
- [3] T. Harada, C.-M. Yoo, K. Kohri, K.-i. Nakao and S. Jhingan, *Primordial black hole formation in the matter-dominated phase of the Universe*, *Astrophys. J.* **833** (2016) 61 [1609.01588].
- [4] S. Passaglia and M. Sasaki, *Primordial black holes from CDM isocurvature perturbations*, *Phys. Rev. D* **105** (2022) 103530 [2109.12824].
- [5] C.-M. Yoo, T. Harada, S. Hirano, H. Okawa and M. Sasaki, *Primordial black hole formation from massless scalar isocurvature*, *Phys. Rev. D* **105** (2022) 103538 [2112.12335].
- [6] M. Y. Khlopov, B. A. Malomed, I. B. Zeldovich and Y. B. Zeldovich, *Gravitational instability of scalar fields and formation of primordial black holes*, *Mon. Not. Roy. Astron. Soc.* **215** (1985) 575.
- [7] J. Martin, T. Papanikolaou and V. Vennin, *Primordial black holes from the preheating instability in single-field inflation*, *JCAP* **01** (2020) 024 [1907.04236].
- [8] B. Carr and F. Kuhnel, *Primordial Black Holes as Dark Matter: Recent Developments*, *Ann. Rev. Nucl. Part. Sci.* **70** (2020) 355 [2006.02838].
- [9] A. M. Green and B. J. Kavanagh, *Primordial Black Holes as a dark matter candidate*, *J. Phys. G* **48** (2021) 043001 [2007.10722].
- [10] B. Carr, K. Kohri, Y. Sendouda and J. Yokoyama, *Constraints on primordial black holes*, *Rept. Prog. Phys.* **84** (2021) 116902 [2002.12778].
- [11] B. Carr and J. Silk, *Primordial Black Holes as Generators of Cosmic Structures*, *Mon. Not. Roy. Astron. Soc.* **478** (2018) 3756 [1801.00672].
- [12] S. Bird, I. Cholis, J. B. Muñoz, Y. Ali-Haïmoud, M. Kamionkowski, E. D. Kovetz et al., *Did LIGO detect dark matter?*, *Phys. Rev. Lett.* **116** (2016) 201301 [1603.00464].
- [13] M. Sasaki, T. Suyama, T. Tanaka and S. Yokoyama, *Primordial Black Hole Scenario for the Gravitational-Wave Event GW150914*, *Phys. Rev. Lett.* **117** (2016) 061101 [1603.08338].
- [14] S. Clesse and J. García-Bellido, *The clustering of massive Primordial Black Holes as Dark Matter: measuring their mass distribution with Advanced LIGO*, *Phys. Dark Univ.* **15** (2017) 142 [1603.05234].
- [15] Q.-G. Huang, C. Yuan, Z.-C. Chen and L. Liu, *GW230529_181500: A Potential Primordial Binary Black Hole Merger in the Mass Gap*, **2404.05691**.
- [16] NANOGrav collaboration, A. Afzal et al., *The NANOGrav 15 yr Data Set: Search for Signals from New Physics*, *Astrophys. J. Lett.* **951** (2023) L11 [2306.16219].
- [17] EPTA, INPTA: collaboration, J. Antoniadis et al., *The second data release from the European Pulsar Timing Array - III. Search for gravitational wave signals*, *Astron. Astrophys.* **678** (2023) A50 [2306.16214].
- [18] D. J. Reardon et al., *Search for an Isotropic Gravitational-wave Background with the Parkes Pulsar Timing Array*, *Astrophys. J. Lett.* **951** (2023) L6 [2306.16215].
- [19] H. Xu et al., *Searching for the Nano-Hertz Stochastic Gravitational Wave Background with the Chinese Pulsar Timing Array Data Release I*, *Res. Astron. Astrophys.* **23** (2023) 075024 [2306.16216].
- [20] B. Carr, S. Clesse and J. García-Bellido, *Primordial black holes from the QCD epoch: Linking dark matter, baryogenesis and anthropic selection*, *Mon. Not. Roy. Astron. Soc.* **501** (2021) 1426 [1904.02129].
- [21] J. García-Bellido, B. Carr and S. Clesse, *Primordial Black Holes and a Common Origin of Baryons and Dark Matter*, *Universe* **8** (2021) 12 [1904.11482].

- [22] E. Despontin, S. Clesse, A. Escrivà and C. Joana, *Were you born in an aborted primordial black hole?*, [2401.09408](#).
- [23] E. Witten, *Searching for a Black Hole in the Outer Solar System*, [2004.14192](#).
- [24] G. Domènech and S. Pi, *NANOGrav hints on planet-mass primordial black holes*, *Sci. China Phys. Mech. Astron.* **65** (2022) 230411 [[2010.03976](#)].
- [25] G. Domènech, *Lectures on Gravitational Wave Signatures of Primordial Black Holes*, 7, 2023, [2307.06964](#).
- [26] LISA collaboration, P. Amaro-Seoane et al., *Laser Interferometer Space Antenna*, [1702.00786](#).
- [27] S. Kawamura et al., *The Japanese space gravitational wave antenna: DECIGO*, *Class. Quant. Grav.* **28** (2011) 094011.
- [28] W.-H. Ruan, Z.-K. Guo, R.-G. Cai and Y.-Z. Zhang, *Taiji program: Gravitational-wave sources*, *Int. J. Mod. Phys. A* **35** (2020) 2050075 [[1807.09495](#)].
- [29] TIANQIN collaboration, J. Luo et al., *TianQin: a space-borne gravitational wave detector*, *Class. Quant. Grav.* **33** (2016) 035010 [[1512.02076](#)].
- [30] R.-g. Cai, S. Pi and M. Sasaki, *Gravitational Waves Induced by non-Gaussian Scalar Perturbations*, *Phys. Rev. Lett.* **122** (2019) 201101 [[1810.11000](#)].
- [31] N. Bartolo, V. De Luca, G. Franciolini, A. Lewis, M. Peloso and A. Riotto, *Primordial Black Hole Dark Matter: LISA Serendipity*, *Phys. Rev. Lett.* **122** (2019) 211301 [[1810.12218](#)].
- [32] C. Unal, *Imprints of Primordial Non-Gaussianity on Gravitational Wave Spectrum*, *Phys. Rev. D* **99** (2019) 041301 [[1811.09151](#)].
- [33] P. Adshead, K. D. Lozanov and Z. J. Weiner, *Non-Gaussianity and the induced gravitational wave background*, *JCAP* **10** (2021) 080 [[2105.01659](#)].
- [34] K. T. Abe, R. Inui, Y. Tada and S. Yokoyama, *Primordial black holes and gravitational waves induced by exponential-tailed perturbations*, *JCAP* **05** (2023) 044 [[2209.13891](#)].
- [35] S. Pi, *Non-Gaussianities in primordial black hole formation and induced gravitational waves*, [2404.06151](#).
- [36] C. Pattison, V. Vennin, H. Assadullahi and D. Wands, *Quantum diffusion during inflation and primordial black holes*, *JCAP* **10** (2017) 046 [[1707.00537](#)].
- [37] J. M. Ezquiaga, J. García-Bellido and V. Vennin, *The exponential tail of inflationary fluctuations: consequences for primordial black holes*, *JCAP* **03** (2020) 029 [[1912.05399](#)].
- [38] D. G. Figueroa, S. Raatikainen, S. Rasanen and E. Tomberg, *Non-Gaussian Tail of the Curvature Perturbation in Stochastic Ultraslow-Roll Inflation: Implications for Primordial Black Hole Production*, *Phys. Rev. Lett.* **127** (2021) 101302 [[2012.06551](#)].
- [39] C. Pattison, V. Vennin, D. Wands and H. Assadullahi, *Ultra-slow-roll inflation with quantum diffusion*, *JCAP* **04** (2021) 080 [[2101.05741](#)].
- [40] V. Atal, J. Garriga and A. Marcos-Caballero, *Primordial black hole formation with non-Gaussian curvature perturbations*, *JCAP* **09** (2019) 073 [[1905.13202](#)].
- [41] V. Atal, J. Cid, A. Escrivà and J. Garriga, *PBH in single field inflation: the effect of shape dispersion and non-Gaussianities*, *JCAP* **05** (2020) 022 [[1908.11357](#)].
- [42] S. Pi and M. Sasaki, *Logarithmic Duality of the Curvature Perturbation*, *Phys. Rev. Lett.* **131** (2023) 011002 [[2211.13932](#)].
- [43] Y. Wang, Q. Gao, S. Gao and Y. Gong, *On the duality in constant-roll inflation*, [2404.18548](#).
- [44] R. Inui, H. Motohashi, S. Pi, Y. Tada and S. Yokoyama, *Constant roll and non-Gaussian tail in light of logarithmic duality*, [2409.13500](#).

- [45] S. Pi and M. Sasaki, *Primordial black hole formation in nonminimal curvaton scenarios*, *Phys. Rev. D* **108** (2023) L101301 [2112.12680].
- [46] H. Motohashi, A. A. Starobinsky and J. Yokoyama, *Inflation with a constant rate of roll*, *JCAP* **09** (2015) 018 [1411.5021].
- [47] H. Motohashi and A. A. Starobinsky, *Constant-roll inflation: confrontation with recent observational data*, *EPL* **117** (2017) 39001 [1702.05847].
- [48] H. Motohashi and A. A. Starobinsky, *Constant-roll inflation in scalar-tensor gravity*, *JCAP* **11** (2019) 025 [1909.10883].
- [49] H. Motohashi and A. A. Starobinsky, *$f(R)$ constant-roll inflation*, *Eur. Phys. J. C* **77** (2017) 538 [1704.08188].
- [50] H. Motohashi, S. Mukohyama and M. Oliosi, *Constant Roll and Primordial Black Holes*, *JCAP* **03** (2020) 002 [1910.13235].
- [51] E. Tomberg, *Stochastic constant-roll inflation and primordial black holes*, *Phys. Rev. D* **108** (2023) 043502 [2304.10903].
- [52] H. Motohashi and Y. Tada, *Squeezed bispectrum and one-loop corrections in transient constant-roll inflation*, *JCAP* **08** (2023) 069 [2303.16035].
- [53] N. Kitajima, Y. Tada, S. Yokoyama and C.-M. Yoo, *Primordial black holes in peak theory with a non-Gaussian tail*, *JCAP* **10** (2021) 053 [2109.00791].
- [54] G. Ferrante, G. Franciolini, A. Iovino, Junior. and A. Urbano, *Primordial non-Gaussianity up to all orders: Theoretical aspects and implications for primordial black hole models*, *Phys. Rev. D* **107** (2023) 043520 [2211.01728].
- [55] C.-M. Yoo, J.-O. Gong and S. Yokoyama, *Abundance of primordial black holes with local non-Gaussianity in peak theory*, *JCAP* **09** (2019) 033 [1906.06790].
- [56] J. M. Bardeen, J. R. Bond, N. Kaiser and A. S. Szalay, *The Statistics of Peaks of Gaussian Random Fields*, *Astrophys. J.* **304** (1986) 15.
- [57] A. Escrivà and C.-M. Yoo, *Non-spherical effects on the mass function of Primordial Black Holes*, **2410.03451**.
- [58] C.-M. Yoo, T. Harada, J. Garriga and K. Kohri, *Primordial black hole abundance from random Gaussian curvature perturbations and a local density threshold*, *PTEP* **2018** (2018) 123E01 [1805.03946].
- [59] C.-M. Yoo, T. Harada, S. Hirano and K. Kohri, *Abundance of Primordial Black Holes in Peak Theory for an Arbitrary Power Spectrum*, *PTEP* **2021** (2021) 013E02 [2008.02425].
- [60] M. Shibata and M. Sasaki, *Black hole formation in the Friedmann universe: Formulation and computation in numerical relativity*, *Phys. Rev. D* **60** (1999) 084002 [gr-qc/9905064].
- [61] T. Harada, C.-M. Yoo, T. Nakama and Y. Koga, *Cosmological long-wavelength solutions and primordial black hole formation*, *Phys. Rev. D* **91** (2015) 084057 [1503.03934].
- [62] A. Escrivà, C. Germani and R. K. Sheth, *Universal threshold for primordial black hole formation*, *Phys. Rev. D* **101** (2020) 044022 [1907.13311].
- [63] K. Uehara, A. Escrivà, T. Harada, D. Saito and C.-M. Yoo, *Numerical simulation of type II primordial black hole formation*, **2401.06329**.
- [64] A. Escrivà, Y. Tada, S. Yokoyama and C.-M. Yoo, *Simulation of primordial black holes with large negative non-Gaussianity*, *JCAP* **05** (2022) 012 [2202.01028].
- [65] T. W. Baumgarte and S. L. Shapiro, *Numerical integration of einstein's field equations*, *Physical Review D* **59** (1998) .

- [66] M. Shibata and T. Nakamura, *Evolution of three-dimensional gravitational waves: Harmonic slicing case*, *Phys. Rev. D* **52** (1995) 5428.
- [67] M. Alcubierre and M. D. Mendez, *Formulations of the 3+1 evolution equations in curvilinear coordinates*, *Gen. Rel. Grav.* **43** (2011) 2769 [[1010.4013](#)].
- [68] M. Alcubierre, *Introduction to 3+1 Numerical Relativity*. Oxford University Press, 04, 2008, [10.1093/acprof:oso/9780199205677.001.0001](#).
- [69] F. Staelens, J. Requier and A. Füzfa, *Universality of the spherical collapse with respect to the matter type : the case of a barotropic fluid with linear equation of state*, *Gen. Rel. Grav.* **53** (2021) 38 [[1912.00677](#)].
- [70] C. W. Misner and D. H. Sharp, *Relativistic equations for adiabatic, spherically symmetric gravitational collapse*, *Phys. Rev.* **136** (1964) B571.
- [71] A. G. Polnarev and I. Musco, *Curvature profiles as initial conditions for primordial black hole formation*, *Class. Quant. Grav.* **24** (2007) 1405 [[gr-qc/0605122](#)].
- [72] A. Escrivà, *Simulation of primordial black hole formation using pseudo-spectral methods*, *Phys. Dark Univ.* **27** (2020) 100466 [[1907.13065](#)].
- [73] V. Vennin, *Stochastic inflation and primordial black holes*, Ph.D. thesis, U. Paris-Saclay, 6, 2020. [2009.08715](#).
- [74] A. Escrivà, V. Atal and J. Garriga, *Formation of trapped vacuum bubbles during inflation, and consequences for PBH scenarios*, *JCAP* **10** (2023) 035 [[2306.09990](#)].
- [75] M. W. Choptuik, *Universality and scaling in gravitational collapse of a massless scalar field*, *Phys. Rev. Lett.* **70** (1993) 9.
- [76] A. M. Abrahams and C. R. Evans, *Critical behavior and scaling in vacuum axisymmetric gravitational collapse*, *Phys. Rev. Lett.* **70** (1993) 2980.
- [77] C. R. Evans and J. S. Coleman, *Observation of critical phenomena and selfsimilarity in the gravitational collapse of radiation fluid*, *Phys. Rev. Lett.* **72** (1994) 1782 [[gr-qc/9402041](#)].
- [78] K. Kohri and T. Terada, *Semianalytic calculation of gravitational wave spectrum nonlinearly induced from primordial curvature perturbations*, *Phys. Rev. D* **97** (2018) 123532 [[1804.08577](#)].
- [79] S. Pi and M. Sasaki, *Gravitational Waves Induced by Scalar Perturbations with a Lognormal Peak*, *JCAP* **09** (2020) 037 [[2005.12306](#)].
- [80] K. Ando, K. Inomata and M. Kawasaki, *Primordial black holes and uncertainties in the choice of the window function*, *Phys. Rev. D* **97** (2018) 103528 [[1802.06393](#)].
- [81] K. Schmitz, *New Sensitivity Curves for Gravitational-Wave Signals from Cosmological Phase Transitions*, *JHEP* **01** (2021) 097 [[2002.04615](#)].
- [82] A. Mitridate, D. Wright, R. von Eckardstein, T. Schröder, J. Nay, K. Olum et al., *PTArcade*, [2306.16377](#).
- [83] G. Franciolini, A. Iovino, Junior., V. Vaskonen and H. Veermae, *Recent Gravitational Wave Observation by Pulsar Timing Arrays and Primordial Black Holes: The Importance of Non-Gaussianities*, *Phys. Rev. Lett.* **131** (2023) 201401 [[2306.17149](#)].
- [84] M. Shimada, A. Escrivà, D. Saito, K. Uehara and C.-M. Yoo, to appear.